Far Infrared Study of IRAS 00494+5617 & IRAS 05327-0457

B. Mookerjea [1], S.K. Ghosh[1], T.N. Rengarajan[1],
S.N. Tandon [2] & R.P. Verma[1]

ABSTRACT

High angular resolution far-infrared observations at 143 & 185 μm, using the TIFR 1-m balloon borne telescope, are presented for two Galactic star forming complexes associated with IRAS 00494+5617 and 05327-0457. The latter map also reveals the cold dust in OMC-3. The HIRES processed IRAS maps at 12, 25, 60 & 100 μm have also been presented for comparison. Both these regions are illuminated at the edges by high mass stars with substantial UV flux.The present study is aimed at quantifying the role of the nearby stars vis-a-vis embedded young stellar objects in the overall heating of these sources. Based on the FIR observations at 143 & 185 μm carried out simultaneously with almost identical angular resolution, reliable dust temperature and optical depth maps have been generated for the brighter regions of these sources. Radiative transfer modeling in spherical geometry has been carried out to extract physical parameters of these sources by considering the observational constraints like : spectral energy distribution, angular size at different wavelengths, dust temperature distribution etc. It has been concluded that for both IRAS 00494+5617 and IRAS 05327-0457, the embedded energy sources play the major role in heating them with finite contribution from the nearby stars. The best fit model for IRAS 00494+5617 is consistent with a simple two phase clump-interclump picture with $\sim 5\%$ volume filling factor (of clumps) and a density contrast of ≈ 80.

Subject Headings: IRAS 00494+5617 – IRAS 05327-0457 – Far Infrared Mapping – Radiative Transfer

1. Introduction

A long term programme of studying the distribution of cold dust (down to $\sim$ 15 K) in and around Galactic star forming regions, is in progress using the 1-m TIFR balloon-borne far-infrared (FIR) telescope. Under this programme, high angular resolution ($\sim 1'$) mapping is carried out simultaneously in two trans-IRAS FIR wavebands (Ghosh et al. 1996; Mookerjea et al. 1998, 1999; Verma et al. 1999). In this paper we present FIR mapping of the sources IRAS 00494+5617 and 05327-0457 in wavebands centered around 143 & 185 μm. These sources share the similarity that each is heated by a luminous external source in addition to one or more possible embedded sources. The simultaneity of observations in the two wavebands with nearly identical beams is useful in deriving reliable temperature distributions of the interstellar dust in these regions.

The source IRAS 00494+5617 is part of the western fragment of the molecular cloud NGC281, located in the Perseus arm at a distance of 2.2 kpc (Cesaroni, Felli & Walmsley 1999). A compact star cluster containing the multiple star HD 5005 as the brightest star excites an ionization front at the edge of NGC 281W. HD 5005 is an O6 V type star and the cluster is at an angular distance of $\sim 5'$ from IRAS 00494+5617. Observational evidences in the form of detection of $C^{34}S$ (3$\rightarrow$2) (Megeath & Wilson 1997), NH_3 (Henning et al. 1994), 22 GHz H_2O masers (Tofani et al. 1995), CO emission (Carpenter, Snell & Schloerb 1990) and molecular outflows (Snell, Dickman & Huang 1990) together with FIR and millimeter continuum emission, strongly suggest ongoing star formation activity in this region. Existing literature on this source suggests that the ongoing star

[1]Tata Institute of Fundamental Research, Homi Bhabha Road, Mumbai 400 005, India

[2]Inter-University Centre for Astronomy & Astrophysics, Ganeshkhind, Pune 411 007, India

formation activity has been induced by the compression due to the propagation of the ionization front (energized by HD 5005) into the molecular cloud (Elmegreen & Lada 1978; Megeath & Wilson 1997). The gas emission features from this source are reasonably well studied. There are not as many high angular resolution observations of the emission from the dust component. Longward of IRAS wavelengths, the only available observations are the high resolution maps at 1.3 mm (Henning et al. 1994).

The source IRAS 05327-0457 is associated with the nebulosity NGC 1977, located near the northern star in the sword of Orion. It is bounded on the south by the northern end of the Orion molecular cloud (Kutner, Evans & Tucker 1976) and is at a distance of 450 pc. The exciting star for the HII region is the B1 V star HD 37018, also known as 42 Ori and is at an angular distance of $\sim 5\farcm9$ from IRAS 05327-0457. Earlier observations of the NGC 1977 region include FIR ($\leq$ 160 μm), near-infrared and radio continuum mapping together with extensive molecular line observations (Makinen et al. 1985; Kutner et al. 1985). High resolution molecular line maps (Kutner et al. 1985) indicate an increase in radial velocity from south to north implying an expansion of the HII region into the molecular cloud, with a velocity of a few km/sec.

In the present study the structural details and dust temperature distributions obtained from FIR observations have been used to quantify the relative contributions of the external and internal sources towards heating these regions. In sections 2 & 3, the observations and the results are described. The discussion including the radiation transfer modeling of these sources is presented in section 4.

2. Observations

2.1. The 143 & 185 μm maps

The Galactic star forming regions associated with the sources IRAS 00494+5617 and 05327-0457 were observed using a two band far-infrared photometer system at the Cassegrain focus of the TIFR 1-m (f/8) balloon-borne telescope. The FIR telescope was flown from the TIFR Balloon Facility, Hyderabad, in central India (Latitude = $17\fdg47$ N , Longitude = $78\fdg57$ E) on 1995 November 12. Details of the telescope and the observational procedure have been given by Ghosh et al. (1988). Additional information specific to this balloon flight has been presented by Mookerjea et al. (1999). The photometer consists of 12 composite silicon bolometers, each having a FOV of $1\farcm6$ and arranged in a 3×2 array for each band. The sky was chopped at 10 Hz by wobbling the secondary mirror. The chopper throw was $4\farcm2$ along the cross elevation axis. The same region of the sky was viewed simultaneously in two bands. The effective wavelengths for the two bands are 143 μm and 185 μm for a greybody spectrum with a temperature of 36 K and λ^{-1} emissivity. All flux densities presented in this paper also use the same assumptions regarding temperature and emissivity. Saturn was observed for absolute flux calibration as well as for the determination of the instrumental Point Spread Function (PSF) including the effect of sky chopping. The absolute flux calibration was done following the method described by Ghosh et al. (1988).

The regions (refer to the Figures 1 and 3) around IRAS 00494+5617 and 05327-0457 were mapped by scanning the sky in cross-elevation with steps in elevation at the end of each scan line. The chopped FIR signals were gridded in a two dimensional sky matrix (elevation & cross elevation) with a cell size of $0\farcm3\times\ 0\farcm3$. The observed chopped signal matrix was deconvolved using an indigenously developed procedure based on the Maximum Entropy Method (MEM) similar to that of Gull & Daniell (1978) (see Ghosh et al. (1988) for details). The FWHM sizes of the deconvolved maps of the point-like source (Saturn) are $1\farcm6\times1\farcm9$ and $1\farcm6\times1\farcm8$ in the 143 and 185 μm bands respectively. An optical photometer at the Cassegrain focal plane was used to improve the absolute positional accuracy of the telescope to $\sim0\farcm5$ (Mookerjea et al. 1999).

2.2. The HIRES processed IRAS maps

To supplement our balloon-borne observations, we have used the IRAS survey data for all four (12, 25, 60 and 100 μm) bands for the regions of the sky around IRAS 00494+5617 and 05327-0457. These data were HIRES processed (Aumann, Fowler & Melnyk 1990) in the Infrared

Processing and Analysis Center (IPAC[1], Caltech) for improving the angular resolutions of the raw maps. These maps have been used to obtain flux densities and angular sizes in the four IRAS bands.

3. Results

3.1. IRAS 00494+5617

Figure 1 shows the intensity maps of the region around IRAS 00494+5617 in the two TIFR and the four IRAS bands. Table 1 presents the coordinates and flux densities (in a circle of $5'$ dia) at all the six wavelengths. The main peak at 185 μm is shifted by $\sim 1'$ compared to the peaks detected at all other wavelengths. The brightest source at 12 μm (IRAS 00492+5614) is too faint in the FIR maps and is not the main source of interest.

The 143 and 185 μm maps show more structural details of the region as compared the 100 μm HIRES map. These maps show extended features (diffuse component) along the east-west direction at low contour levels. The presence of a diffuse component is also noticed in all the HIRES maps. The FIR maps presented here have the shape of a peanut, similar to the shape at 1.3 mm observed by Henning et al. (1994).

In addition to the diffuse component, the 143 μm map shows a secondary peak (S2) towards the west; this is not seen in the maps of other bands. The position and flux density (after correcting for the diffuse emission) of S2 at 143 μm are also presented in Table 1. The limits in the other bands refer to the flux densities measured in a circle ($2'$ dia) centered at the position of S2 at 143 μm. Although the HIRES maps do not detect S2, the HIRAS map at 60 μm processed with the Groningen IRAS Software Telescope (Henning et al. 1994) with better angular resolution indicates the presence of the same.

Figure 2 presents the contour maps of the temperature (T(143/185)) and optical depth (τ_{150}) for this region, generated using the method described by Mookerjea et al. (1999). For these maps a dust emissivity, $\epsilon_\lambda \propto \lambda^{-1}$ has been assumed. The temperatures determined are accurate to within $\pm$ 2 K between 20 and 50 K and within $\sim \pm$ 5 K between 50 and 75 K. The structural details in these maps are highly reliable due to (i) the simultaneity of observations and (ii) conservative processing e.g., 3 pixel by 3 pixel smoothing of the flux densities done prior to the determination of the temperature. The temperature and optical depth maps have been restricted to the regions where the intensities in both the wavebands are substantially higher (> 10 times) than the measured noise level. From the temperature map it is seen that there are two regions of enhancement close to the boundary, the highest temperature being close to the boundary facing HD 5005. Further, the temperature distribution seems to be featureless over most of the central region and shows a minimum near the center. In contrast, the peak of the τ_{150} map coincides with the peak at 185 μm and the contours decrease smoothly outwards, as in the intensity map.

3.2. IRAS 05327-0457

Figure 3 presents the intensity maps of the region surrounding IRAS 05327-0457 in the six wavebands considered in this paper. The positions of the global peak in the 143 & 185 μm maps agree with the IRAS Point Source Catalog (PSC) coordinates within the achieved absolute positional accuracy in the maps. The source is extended along a direction approximately perpendicular to the line joining the cloud to the star 42 Ori. The basic features of the intensity distributions at 143 and 185 μm are similar to the 60 and 100 μm HIRES maps as well as the 158 μm [C II] maps by Howe et al. (1991). The emission due to 42 Ori (located to the north of IRAS 05327-0457) is clearly seen in the 12 and 25 μm maps. Table 2 presents the position and flux densities in a circle of $5'$ dia centered on the global peak in each of the six wavebands.

In both the 143 and 185 μm maps, a fainter source (P2) is detected towards the south of IRAS 05327-0457. Positionally this matches very well with the coldest sub-millimeter source (CSO 10) detected at 350 μm by Lis et al. (1998). This is associated with the Orion Molecular Cloud -3 and has also been detected at 1.3 mm by Chini et al. (1997). The dust temperature, T(143/185) for P2 has been estimated to be $\sim$ 19 K assuming $\epsilon_\lambda \propto \lambda^{-2}$, the choice of the dust emissivity index being guided by Lis et al. (1998). This low temperature source is not detected in any of the HIRES maps.

[1]IPAC is funded by NASA as part of the part of the IRAS extended mission program under contract to JPL.

Table 2 presents the position and flux densities of P2.

Figure 4 shows the maps of the dust temperature (T(143/185)) and optical depth (τ_{150}) for IRAS 05327-0457, generated using same methods as for IRAS 00494+5617. In the τ_{150} map, the peak has a value of 0.02 and is shifted, north-east towards the direction of the ionizing star. The optical depth decreases monotonically towards the south-west. Higher temperatures are seen towards the south-eastern and western edges; rest of the region is seen to have smoothly varying temperatures, between 25 and 35 K. There is no increase in the dust temperature near the edge facing 42 Ori. The T(143/185) and the τ_{150} map together suggest the presence of (i) embedded sources of heating at the positions of temperature enhancements and (ii) a high density shell facing 42 Ori.

4. Discussion

4.1. Radiation transfer scheme & Models explored

We have explored the major sources of dust heating based on radiation transfer modeling of the sources. The radiation transfer equations have been solved assuming a 2-point boundary condition for a spherically symmetric cloud of dust and gas. Based on the boundary conditions, we have constructed 3 types of models : *model A* – the cloud is heated by centrally embedded sources and by an external radiation field due to the average Galactic Interstellar Radiation Field (ISRF) and nearby stars; *model B* - the cloud is heated by internal sources and ISRF only; *model C* – there is no embedded source, the cloud is heated only externally by the ISRF and radiation due to nearby stars. The contribution of the nearby star in the models A and C has been calculated in the following way: the geometrically diluted stellar radiation intercepted by the cloud surface is estimated and it is then smeared out uniformly over the entire surface of the cloud. This calculated contribution could be a slight overestimate since the absorption in the intervening medium has been neglected. For modeling the observed Spectral Energy Distribution (SED) two types of dust have been considered. The dust properties have been taken from two sources viz., Draine & Lee (1984) (hereafter DL) and Mezger, Mathis & Panagia, (1982) (hereafter MMP). The dust compositions include mixtures of astronomical silicate and graphite. For the DL type of dust grains, size averaged properties are used taking a size distribution of $n(a)da \sim a^{-3.5}da$ (Mathis, Rumpl & Nordsieck 1977), with a ranging between 0.01 and 0.25 μm. The average Galactic ISRF used for this problem has been taken from Mathis, Mezger & Panagia (1983). The cloud is parameterized by the following physical quantities: R_{max}, the outer size of the cloud, R_{min}, the radius of the inner dust cavity, τ_{100}, the total radial optical depth at 100 μm and the radial dust (hence gas) density distribution (r^{β}, β=0, -1, -2). The contributions of ISRF and the external source (if any) are kept fixed, while the luminosity of the embedded source, the dust composition, τ_{100} value and radial distribution of the dust density and the physical sizes of the cloud are varied to obtain a good match to observations. The gas to dust ratio has been assumed to be 100:1 by mass. Using this scheme a best fit model matching the observed spectral energy distributions (SED), radial profiles at selected wavelengths and the radio continuum flux are obtained. These radiation transfer calculations have been done using a modified version of the code CSDUST3 (Egan, Leung & Spagna 1988), which is capable of treating gas and dust in a self-consistent manner (Mookerjea et al. 1999; Mookerjea & Ghosh 1999).

In the following subsections we explore the tenability of the models A, B and C in the light of available observational constraints for individual sources.

4.2. IRAS 00494+5617

4.2.1. The main source

The observed SED for the source IRAS 00494+5617 has been constructed using the flux densities presented in Table 1 along with flux densities at 1.3 mm (Henning et al. 1994) and 2.9 mm (Walker, Adams & Lada 1990). The total observed luminosity is 2.4×10^4 $L_{\odot}$ (Carpenter, Snell & Schloerb 1990) and no radio continuum emission is detected at 8.4 GHz (Tofani et al. 1995) from this cloud. T(143/185) map shows enhanced temperature towards the boundary closer to HD 5005. In order to explain these, the embedded source in radiation transfer models A and B is assumed to be a

cluster of stars. In models A and C an intercepted luminosity of $6.9\times10^3 L_\odot$ from HD 5005 has been considered. For each type of model it is found that the best fit is obtained for the case of uniform density and grains of DL type. Figure 5 shows the observed and the best fit SEDs. Model A fits the SED at all wavelengths very well, while model B shows some mid-infrared excess. Model C fails to reproduce any of the observed flux densities. The predicted radial profiles (as obtained by convolving the model profiles with instrumental PSFs) for the models A and B are almost similar. Table 3 compares the FWHMs predicted by model A with those observed at 25, 60, 100, 143 and 185 μm. The observed FWHMs presented here refer to the FWHMs for the source along its major and the minor axes. We find that model A not only fits the observed SED better than model B but also achieves an overall consistency by supporting the role of HD 5005 in heating the cloud and fitting the observed FWHMs reasonably well. Table 4 presents the parameters of the best fit model A for this source alongwith the uncertainties in the τ_{100} and the embedded luminosity. These uncertainties have been estimated using only the SED fit and keeping the other parameters fixed. From this radiation transfer modeling and the T(143/185) map we conclude that the source IRAS 00494+5617 is primarily heated by one or more embedded sources with non-negligible contribution from HD 5005.

We compare he FWHM predicted from the best fit spherically symmetric model with the observed FWHM along the minor axis. For IRAS 00494+5617 we find that at 100, 143 and 185 μm model predictions for FWHMs match the observed FWHMs (along minor axis) fairly well. However at 25 μm (which traces much hotter dust) the observed FWHM is substantially larger than the model prediction. This trend is also seen at 60 μm, though not to the same extent as at 25 μm. This can be explained by invoking spatially distributed heating sources embedded in clumps. It may be noted that our dust temperature maps also shows the presence of two temperature enhancements. This clumpiness is also substantiated by high resolution $C^{18}O$ observations by Megeath & Wilson (1997), which have revealed that this western fragment of NGC 281 is composed of three clumps. The best fit model A obtained above corresponds to a gas density of 2.2×10^4 cm^{-3} (for a gas to dust density of 100:1 by mass) and a total mass of $1890 M_\odot$. Megeath & Wilson (1997) obtain $1080 M_\odot$ as the lower limit for the total mass in the three clumps. The residual mass (810 $M_\odot$) as predicted by the model can be present in the form of the inter-clump medium. The projected radii (taking the distance to the source to be 2.9 kpc) of the clumps were given by Megeath & Wilson (1997) assuming the clumps to be spherical. We assume that all three clumps are spherical and are confined within the boundary of the spherical model A above. After scaling the clump sizes to our assumed distance of 2.2 kpc, we find that the volume filling factor is 4.5 %. Using the total mass from our model A and assuming an interclump medium of uniform density we obtain a value of 4.5×10^3 cm^{-3} for the number density of the interclump medium. We also calculate the clump-interclump density contrast to be $\sim$ 80. The resultant clump density of 3×10^5 cm^{-3} is consistent with the detection of $C^{34}S$. Although the estimates presented here are based on crude approximations, the values for filling factors of clumps and clump-interclump density contrast obtained here can be called very typical, while comparing with the measured values of such parameters for other clumped sources (Howe et al. 1991).

4.2.2. Diffuse emission

The 143 μm map of this region shows a considerable amount of diffuse emission particularly towards the west. This emission is to a certain extent positionally coincident and structurally similar to that in the 185 μm map. We have looked into the possible energy sources for this emission. The flux densities (in an aperture of 2$'$ dia centered at $0^h\ 49^m\ 09^s$ $+56^\circ\ 17'\ 30''$ (1950)) at 143 and 185 μm are 236 and 265 Jy respectively. The bolometric luminosity of the diffuse emission over a diameter of 2$'$ has been estimated to be $\sim$ 870 $L_\odot$. This luminosity cannot be explained due to heating by either the the average ISRF or the star cluster HD 5005. We explore the possibility of radiation actually leaking from the main source (around 00494+5617) and heating the dust in the neighbourhood. Under this assumption we obtain that about 8% of the total luminosity of the embedded source would have to be intercepted by the region where diffuse emission is detected. The separation between the region of diffuse emission

and IRAS 00494+5617 is such that the solid angle covered by the diffuse region is adequate to intercept the requisite amount of radiation. This evidence of luminosity leakage further supports the presence of clumpiness discussed in Section 4.2.1.

4.3. IRAS 05327-0457

The observed SED for the region around IRAS 05327-0457 has been constructed using the flux densities presented in Table 2 alongwith the IRAS Low Resolution spectrum (LRS) (Chen, Gao & Xiong 1995). VLA observations of this source by Kutner et al. (1985) have not detected any radio continuum emission at 5 GHz and from the detection limit predict the embedded source to be a ZAMS B2.5 or later type star. Based on their observations Kutner et al. (1985) have suggested that 42 Ori plays the most significant role in fueling the FIR emission from this source. However the T(143/185) map presented here shows no temperature enhancement towards the boundary illuminated by the star 42 Ori. It rather shows an increase from the boundary towards the position of IRAS 05327-0457.

We have applied the radiation transfer models *A*, *B* and *C* (see Section 4.1) to IRAS 05327-0457. The embedded source for models of type *A* and *B* is taken to be a star of type B2. In models of types *A* and *C* the intercepted contribution of $600 L_{\odot}$ from 42 Ori is considered. Figure 6 presents the SEDs predicted from the models *A*, *B* and *C* in comparison with the observations. The model outputs shown are the best fits for each type. As in the case of IRAS 00494+5617 uniform density gives the best fit for all three models. Further the MMP type grains lead to better fit than the DL type grains. While the predicted SED from model *A* matches the observations at all wavelengths reasonably well, model *B* predicts fluxes less than the observed values longward of 60 μm. Predictions from model *C* do not the fit the observations at all. The predicted FWHMs (post convolution) are similar for models of type *A* and *B*. Table 3 presents the comparison of FWHM sizes from model *A* at different wavelengths with observations. From model *A* the predicted radio continuum emission at 5 GHz is $\sim$14 mJy which is well above the sensitivity of the VLA observations by Kutner et al. (1985). The reasons for this non-detection could be : (i) the embedded source is a cluster of stars (with masses less than that of a B2 star) with combined luminosity equal to that of a B2 star. This is supported by the detection of multiple stars in the near-infrared (Makinen et al. 1985). They have detected 7 stars having a total luminosity of $2.3{\times}10^3 L_{\odot}$ (model *A* total luminosity = $2.8{\times}10^3 L_{\odot}$). Our temperature map also indicates presence of two sources, again close to the boundary. (ii) Since the radio continuum emission has a strong n_e^2 dependence, a smaller gas to dust ratio could explain the reduced emission. (iii) The radio emission could largely be attenuated by free-free absorption. The third possibility proposed would arise, if the gas density distribution very close to the star ($r << R_{min}$) is r^{-2}, a typical situation for ionized wind.

Of the models presented here, model *A* explains the observed SED, the radial profile, the T(143/185) map and the role of 42 Ori in heating the cloud most satisfactorily. Table 4 presents the parameters of this model and the estimated uncertainties in the embedded luminosity and τ_{100}. From radiation transfer modeling we conclude that it is absolutely necessary to have an embedded source to explain the total emission from IRAS 05327-0457. Clearly 42 Ori cannot be the only heating source since the luminosity intercepted by IRAS 05327-0457 is $\leq$ 20 % of the observed luminosity. Further we have verified that the temperature profile from radiation transfer calculation using a slab geometry and 42 Ori as the source, does not fit observations.

The observed angular sizes for IRAS 05327-0457 at 100 μm and more prominently at 60 μm are larger than the model values. As in IRAS 00494+5617 this is again consistent with a distribution of embedded hot sources as suggested by the T(143/185) map (Figure 4) as well. The apparent reduction in the observed FWHMs at 143 and 185 μm as compared to the FWHM at 100 μm could be due to the effect of sky chopping.

5. Summary

This paper presents simultaneous far-infrared mapping observations at 143 and 185 μm of the regions around IRAS 00494+5617 and IRAS 05327-0457. Both sources have been well resolved at these wavelengths. The cold dust source CSO 10 located in OMC-3 (Lis et al. 1998) has also

been detected in our map of IRAS 05327-0457. HIRES processed IRAS maps in all 4 bands have been used for comparison. Reliable dust temperature (T(143/185)) and optical depth (τ_{150}) maps for these sources are presented. Radiation transfer models have been constructed to explain the observed SEDs, radial profile and the influence of external heating agencies for both these sources. These models provide useful physical parameters for the star forming clouds associated with these sources. For both IRAS 00494+5617 and 05327-0457 it has been demonstrated that although HD 5005 and 42 Ori contribute to their heating respectively, it is necessary to have dominant contribution from embedded sources to explain the observed SEDs. Comparison of predicted radial profiles from models with observations suggest presence of a distribution of embedded clumps in both sources. This is corroborated by spatially resolved peaks in the maps of dust temperature. A simplistic model for the clumpiness of IRAS 00494+5617 has been proposed based on parameters derived from radiation transfer models and previous molecular line observations.

It is a pleasure to thank all members of the Infrared Astronomy Group of T.I.F.R. for their support during laboratory tests and balloon flight campaigns. All members of the Balloon Group and Control Instrumentation Group of the TIFR Balloon Facility, Hyderabad, are thanked for their technical support during the flight. We thank IPAC, Caltech, for providing us the HIRES processed IRAS products. We thank the anonymous referee for the suggestions which have improved the quality of the paper.

REFERENCES

Aumann H.H., Fowler J.W. & Melnyk M. 1990, AJ, 99, 1674

Carpenter, J. M., Snell, R. L. & Schloerb, F. P. 1990, ApJ, 362, 147

Cesaroni, R., Felli, M. & Walmsley, C. M. 1999, A&AS, 136, 333

Chen, P. S., Gao H. & Xiong, G. Z. 1995, ApJS, 100, 389

Chini, R., Reipurth, B., Ward-Thompson, D. , Bally, J., Nyman, L. -A, Sievers, A. & Billawala, Y. 1997, ApJ, 474, L135

Draine, B. T. & Lee, H. M. 1984, ApJ, 285, 89

Egan, M. P., Leung, C. M., Spagna, G. F. 1988, Computer Physics Communications, 48, 271

Elmegreen, B. G. & Lada, C. J. 1978, ApJ, 219, 467

Ghosh, S. K., Iyengar, K. V. K, Rengarajan, T. N., Tandon, S. N., Verma, R. P. & Daniel, R. R. 1988, ApJ, 330, 928

Ghosh, S. K., Rengarajan, T. N., Verma, R. P. & Karnik, A.D. 1996, "Interplay between Massive Star Formation, the ISM and Galaxy Evolution", Proc. of 11th IAP Astrophysics Meeting, p499

Gull, S. F. & Daniell, G. J. 1978, Nature, 272, 686

Henning, Th., Martin, K., Reimann, H. -G., Launhardt, R., Leisawitz, D. & Zinnecker, H. 1994, A&A, 288, 282

Howe, J. E., Jaffe, D. T., Genzel, R. & Stacey, G. J. 1991, ApJ, 373, 158

Kutner, M. L., Machnik, D. E., Mead, K. N. & Evans, N. J. 1985, ApJ, 299, 351

Kutner, M. L., Evans, N. J., Tucker, K. D. 1976, ApJ, 209, 452

Lis, D. C., Serabyn, E., Keene, J., Dowell, C. D., Benford, D. J., Phillips, T. G., Hunter, T. R. & Wang, N. 1998, ApJ, 509, 299

Makinen, P., Harvey, P. M., Wilking, B. A. & Evans, N. J. 1985, ApJ, 299, 341

Mathis, J. S., Mezger, P. G., Panagia, N. 1983, A & A, 128, 212

Mathis, J. S., Rumpl, W., Nordsieck, K. H. 1977, ApJ, 217, 425

Mezger, P. G., Mathis, J. S., Panagia, N. 1982, A & A, 105, 372

Megeath, S. T. & Wilson, T. L. 1997, AJ, 114, 1106

Mookerjea B., Ghosh S.K., Karnik A.D., Rengarajan T.N., Tandon S.N. & Verma R.P. 1998, Bull. Astron. Soc. India, 27, 155

Mookerjea B., Ghosh S.K., Karnik A.D., Rengarajan T.N., Tandon S.N. & Verma R.P. 1999, ApJ, 522, 285

Mookerjea B. & Ghosh S.K. 1999, J. Astrophys. & Astron., 20, 1

Snell, R. L., Dickman, R. L. & Huang, Y. -L. 1990, ApJ, 352, 139

Tofani, G., Felli, M., Taylor, G. B. & Hunter, T.R. 1995, A&AS, 112, 299

Verma, R. P., Ghosh, S. K., Karnik, A. D., Mookerjea, B., & Rengarajan, T. N. 1999, "The Universe as seen by ISO", ESA Special Publication SP-427 (ed. P. Cox)

Walker, C. K., Adams, F. C. & Lada, C. J. 1990, ApJ, 349, 515

Fig. 1.— The intensity maps for the region around IRAS 00494+5617 : (a) at 185 μm with peak = 644 Jy/sq. arcmin with contour levels =95, 90, 80, 70, 60, 50, 40, 30, 20, 10, 7.5 % of the peak; (b) at 143 μm with peak = 341 Jy/ sq. arcmin. Contour levels in (b) are same as in (a) but upto 20 % of the peak. "$*$" shows the position of HD 5005. The lowest contour for each map is $\sim$ 5 times the noise level. The insets show deconvolved images of Saturn in the respective bands, aligned to the instrumental axes for meaningful comparison. The contours for Saturn denote 90, 70 and 50 % of respective peaks. HIRES processed IRAS maps at (c) 100 μm, (d) 60 μm, (e) 25 μm and (f) 12 μm, with contours at levels same as in (a) but upto 10% of the respective peaks. The peak values in these bands are 302, 173, 20.9 and 5.6 Jy /sq. arcmin respectively. The resolutions at 12, 25, 60 and 100 μm are $0\farcm9\times0\farcm45$, $0\farcm7\times0\farcm45$, $1\farcm3\times0\farcm8$ and $2\farcm0\times1\farcm6$ respectively .

Fig. 2.— (a) The dust temperature, $T(143/185)$ and (b) optical depth τ_{150}, maps respectively for the region near IRAS 00494+5617 for $\epsilon_\lambda \propto \lambda^{-1}$ emissivity law. The contours in (a) are at 70, 60, 50, 45, 40, 35, 30, 25, 20 & 16 K. The contours in (b) are at 95, 90, 80, 70, 60, 50, 40, 30, 20, 10, 5, 2.5, 1% of the peak (0.15).

Fig. 3.— The intensity maps for the region around IRAS 05327-0457 : (a) at 185 μm with peak = 548 Jy/ sq. arcmin and (b) at 143 μm with peak = 681 Jy/ sq. arcmin."+1" shows the IRAS PSC position of the source, "+2" shows the position of the source CSO 10 (Lis et al., 1998) and "$*$" shows the position of 42 Ori.The lowest contour is $\sim$ 5 times the noise level. Insets are same as in Fig. 1(a) and (b). HIRES processed IRAS maps at (c) 100 μm, (d) 60 μm, (e) 25 μm and (f) 12 μm. with contours at levels same as the top 9 levels of Fig. 1 (a). The peak values in these bands are 802, 688, 83.9 and 25.5 Jy /sq. arcmin respectively. Contours levels at all wavelengths are same fractions of the respective peaks as in Figure 1(b). The angular resolution at 12, 25, 60 and 100 μm are $1\farcm0\times0\farcm3$, $1\farcm1\times0\farcm6$, $1\farcm6\times1\farcm1$ and $2\farcm2\times2\farcm0$ respectively.

Fig. 4.— (a) The dust temperature $T(143/185)$ and (b) optical depth τ_{150} maps respectively for the region near IRAS 05327-0457 for $\epsilon_\lambda \propto \lambda^{-1}$ emissivity law. The contours in (a) are at 70, 60, 50, 45, 40, 35, 30, 25, 20 & 15 K. The contours in (b) as percentages of the peak value of 0.02 are same as the top 10 levels of Fig. 2(b).

Fig. 5.— Comparison of the observed spectral energy distribution with the predictions from the models explored (see text) for IRAS 00494+5617. *A* is the best fit model.

Fig. 6.— Comparison of the observed spectral energy distribution with the predictions from the models explored (see text) for IRAS 05327-0457. *A* is the best fit model.

This 2-column preprint was prepared with the AAS LaTeX macros v5.0.

TABLE 1

POSITIONS AND FLUX DENSITIES OF THE DETECTED SOURCES IN THE REGION AROUND IRAS 00494+5617

Source	λ μm	Position α_{1950} 0^h	δ_{1950} $+56^\circ$	Flux Density Jy[a]
	12	$49^m\ 24\overset{s}{.}8$	$17'\ 42''$	35
	25	49 28.4	17 27	70
	60	49 30.2	17 42	733
S 1	100	49 26.6	17 27	1762
	143	49 29.9	17 22	2460
	185	49 27.8	16 31	2820
S 2	143	48 44.6	16 39	115[b]
	60	"	"	<25[b]
	100	"	"	<60[b]
	185	"	"	<110[b]

[a]Flux density in 5′ diameter circle unless otherwise stated

[b]Flux density in 2′ diameter circle

TABLE 2

POSITIONS AND FLUX DENSITIES OF THE DETECTED SOURCES IN THE REGION AROUND IRAS 05327-0457

Source	λ μm	Position α_{1950} $5^h\ 32^m$	δ_{1950}	Flux Density Jy[a]	Comment
	12	$46\overset{s}{.}9$	- 4° 57′ 28″	191	
	25	45.9	- 4 57 43	383	IRAS
P 1	60	45.9	- 4 56 58	5401	05327-0457
	100	45.9	- 4 56 58	7896	
	143	45.4	- 4 57 47	5350	
	185	46.4	- 4 57 38	3810	
P 2	143	$56\overset{s}{.}6$	- 5 03 50	580[b]	MMS 6
	185	$57\overset{s}{.}0$	- 5 03 25	1820[c]	

[a]Flux density in 5′ diameter circle unless otherwise stated

[b]Flux density in 2′ diameter circle

[c]Flux density in 3′ diameter circle

Table 3

Comparison of model predictions of FWHMs with observations.

Source	λ μm	Model	Observations (major×minor)
IRAS 00494+5617	25	0.′6	1.′8×1.′6
	60	1.′0	2.′6×1.′8
	100	2.′2	2.′3×2.′0
	143	2.′3	3.′4×2.′3
	185	2.′5	2.′3×1.′8
IRAS 05327-0457	60	1.′5	5.′5×2.′2
	100	2.′8	7.′3×3.′1
	143	2.′7	5.′0×1.′8
	185	3.′0	3.′2×1.′9

Table 4

Parameters for the best fit radiation transfer model

Source	β	R_{max} (pc)	R_{min} (pc)	Dust type	τ_{100}	Luminosity (10^3 $L_\odot$)	Dust Composition Silicate:Graphite % : %
IRAS 00494+5617	0.0	1.2	0.0001	DL[a]	0.1±0.01	12±2	32:68
IRAS 05327-0457	0.0	0.35	0.0001	MMP[b]	0.03±0.005	2.8±0.2	11:89

[a]DL - Draine & Lee (1984).

[b]MMP - Mathis, Mezger & Panagia (1983).

IRAS 00494+5617

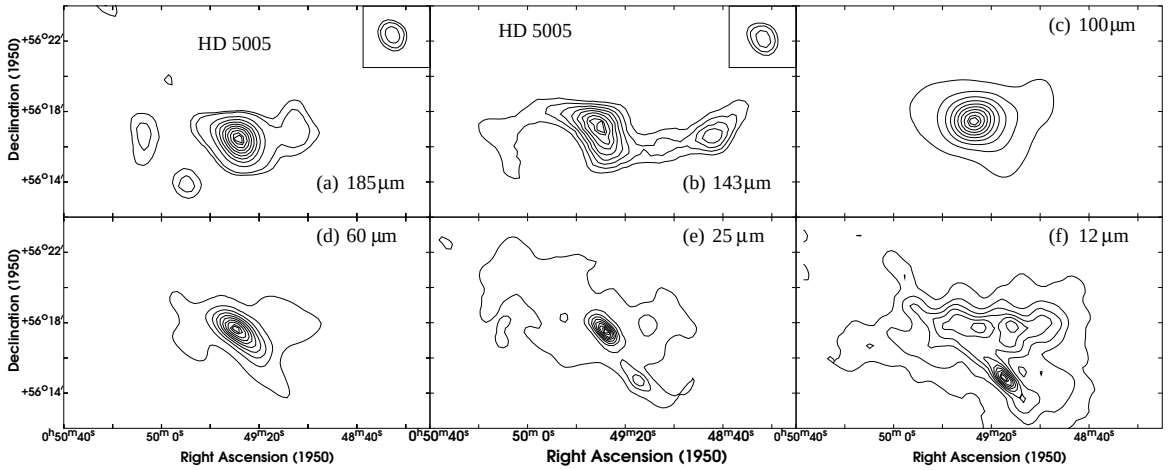

IRAS 00494+5617

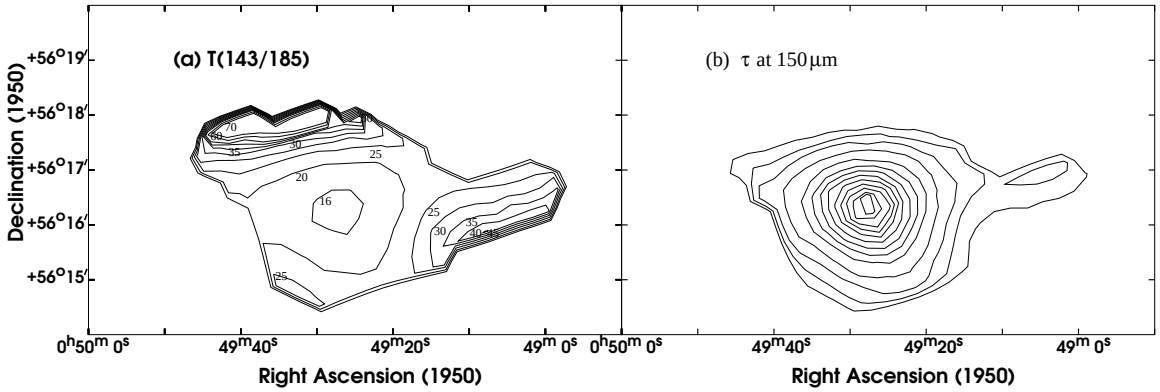

IRAS 05327-0457

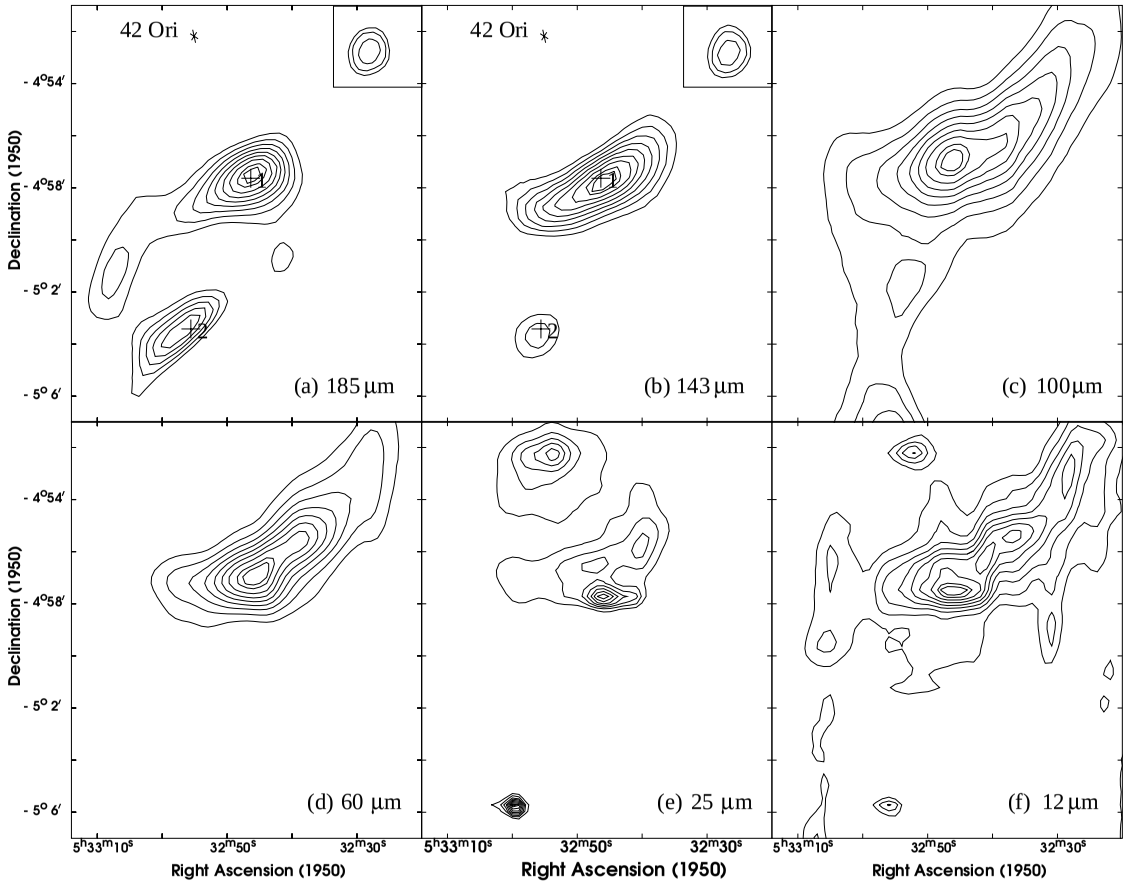

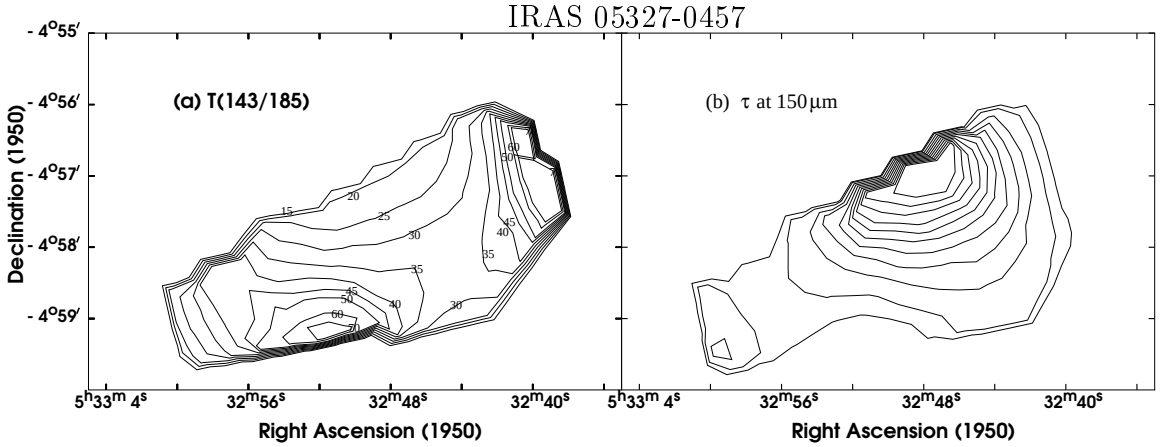
IRAS 05327-0457
(a) T(143/185)
(b) τ at 150μm
Declination (1950)
- 4°55′
- 4°56′
- 4°57′
- 4°58′
- 4°59′
5h33m 4s
32m56s
32m48s
32m40s
Right Ascension (1950)
15
20
25
30
35
40
45
50
60
70
80

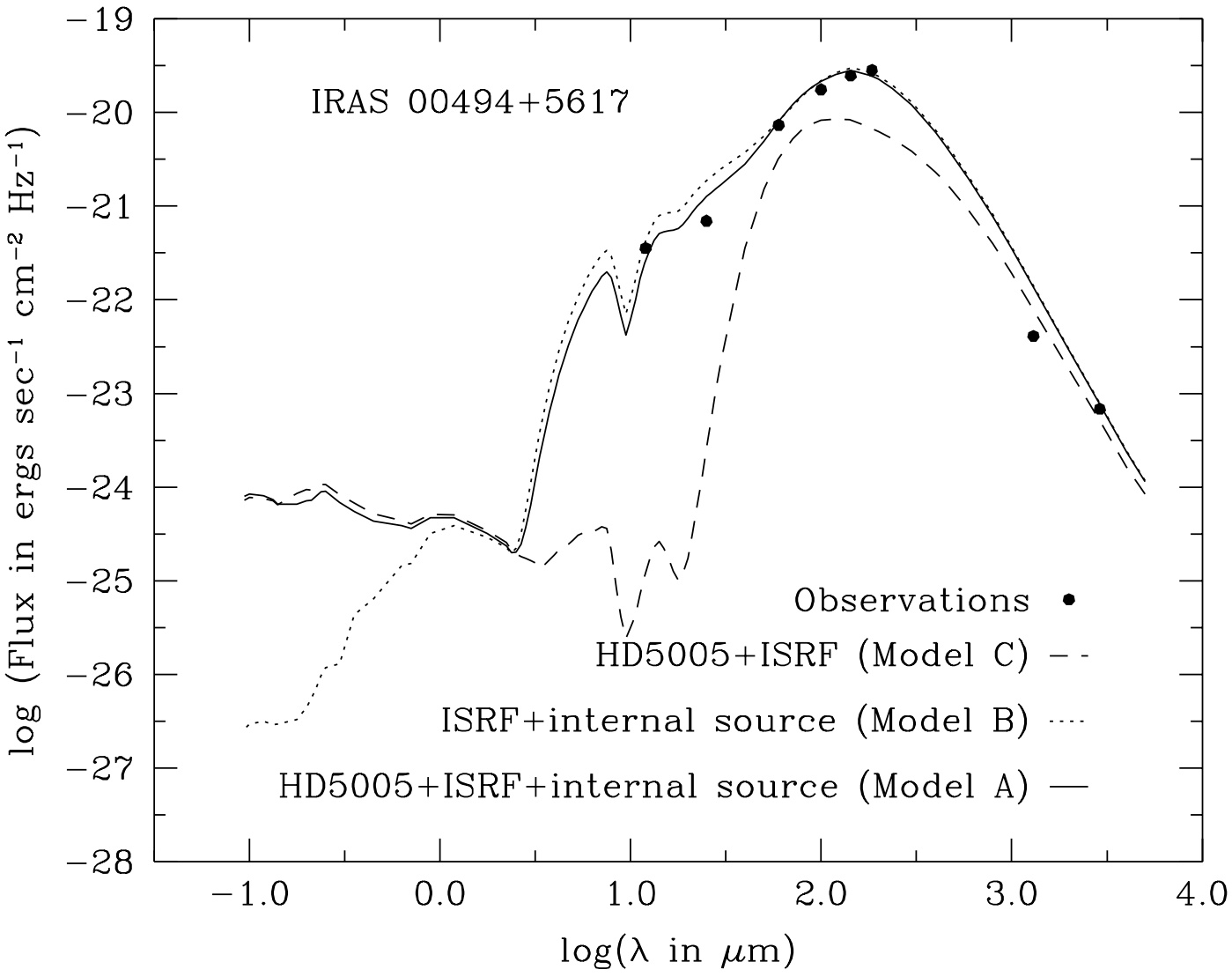
IRAS 00494+5617
Observations
HD5005+ISRF (Model C)
ISRF+internal source (Model B)
HD5005+ISRF+internal source (Model A)
log (Flux in ergs sec^{-1} cm^{-2} Hz^{-1})
log(λ in μm)
−19
−20
−21
−22
−23
−24
−25
−26
−27
−28
−1.0
0.0
1.0
2.0
3.0
4.0

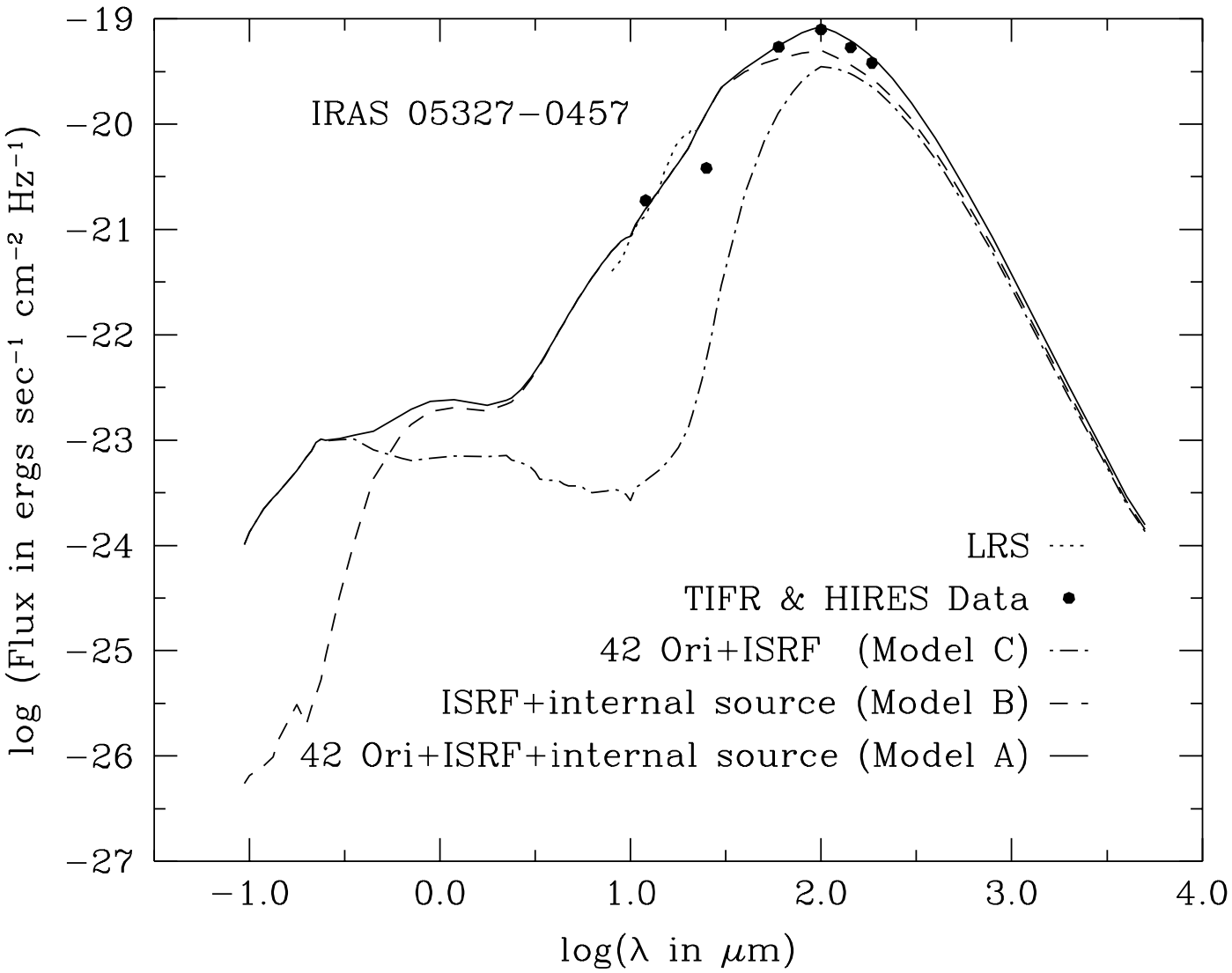
IRAS 05327−0457
LRS
TIFR & HIRES Data
42 Ori+ISRF (Model C)
ISRF+internal source (Model B)
42 Ori+ISRF+internal source (Model A)
log (Flux in ergs sec⁻¹ cm⁻² Hz⁻¹)
log(λ in μm)
−19
−20
−21
−22
−23
−24
−25
−26
−27
−1.0
0.0
1.0
2.0
3.0
4.0